

Full Length Article

Ternary cobalt–iron sulfide as a robust electrocatalyst for water oxidation: A dual effect from surface evolution and metal doping

Ali Naderi^a, Xue Yong^b, Mohammadreza Karamad^c, Jinyan Cai^{a,*}, Yipeng Zang^a, Ian Gates^c, Samira Siahrostami^{b,*}, Gongming Wang^{a,*}

^a Department of Chemistry, University of Science and Technology of China, Hefei, Anhui 230026, China

^b Department of Chemistry, University of Calgary, 2500 University Drive NW, Calgary, Alberta T2N 1N4, Canada

^c Department of Chemical and Petroleum Engineering, University of Calgary, 2500 University Drive NW, Calgary, Alberta T2N 1N4, Canada



ARTICLE INFO

Keywords:

Oxygen evolution reaction
Cobalt/Iron Disulfide
Iron concentration effect
Density functional theory
Overpotential

ABSTRACT

Water electrolysis is considered as a promising sustainable technology to produce hydrogen thereby reducing dependence on fossil fuels. The oxygen evolution reaction (OER), a half reaction of water electrolysis is hampered by its slow kinetics. Developing high performance electrocatalysts for enhancing OER kinetics is the main bottleneck of this technology. In this study, we synthesize a ternary cobalt iron disulfide as a pre-catalyst for OER. After the activation step, the synthesized catalyst transformed to cobalt-iron amorphous oxide with oxygen defects as an efficient catalyst for OER. At its optimized Co/Fe ratio, equal to 3:1, the activated catalyst requires only 267 mV overpotential to reach the current density of 10 mA cm⁻², while Tafel slope is 34 mV dec⁻¹. Density functional theory calculation reveals that the active phase of the OER process is a thin layer of oxide that forms during the voltammetry activating process and the reduced energy barrier of rate determining step contributes to the excellent OER performance of cobalt-iron amorphous oxide.

1. Introduction

Increasing energy demands and environment pollutions caused by fossil fuel consumption have made exploitation of sustainable energy sources inevitable and crucial [1]. One of the most promising energy technologies, proposed in this regard, is water splitting powered by electricity to produce clean hydrogen (H₂). However, this system suffers from significant shortcomings, namely the slow kinetics of the oxygen evolution reaction (OER) which occurs at the anode of the electrolytic cell, and corrosion of the electrode in acidic media [2]. Developing high efficient alkaline OER electrocatalyst has been one of focal points in this field [1]. Till now, Ru/Ir-based materials are state-of-the-art catalysts for the water oxidation reaction. However, their usage is limited by their high cost and scarcity [3,4]. Finding low cost and efficient materials are required for feasible sustainable water-electrolysis technologies [3–5].

Co-based materials are earth abundant and promising materials as efficient non-noble metal catalysts for OER [6]. However, they suffer from low activity and durability which hinder their abilities as highly efficient nonprecious OER catalysts [6]. So far, a great deal of effort has been made to overcome this problem. For example, cobalt oxides [7–9]

cobalt nitrides [10,11], cobalt phosphides [12,13], and cobalt chalcogenides [14–18] have been examined in the literature. The results demonstrate that cobalt chalcogenides are among the most promising electrocatalysts for OER. The key advantages of these compounds are their higher conductivities and greater thermal and chemical stability [3,4]. Additionally, they are better catalysts for OER as their surface defects and more exposed active sites which are the result of amorphous or porous structures that formed after the activation steps [19]. However, they still perform lower than Ru/Ir-based catalysts. Thus, it is crucial to design high-performance Co chalcogenides, which have comparable activity and durability to Ru/Ir-based catalysts. Recent studies have demonstrated that iron acts to promote the catalytic activity of cobalt-based compounds. Burke et al. revealed that iron raises the intrinsic activity of cobalt oxy (hydroxide) by creating new active sites [20]. Zhang et al. compared two modes of Fe incorporation in Co-Fe (oxy)hydroxide and found Co and Fe co-deposition result in higher OER catalytic activity and stability than CoO_xH_y [21]. Other researches also show that iron plays an important role in enhancing OER activity of cobalt oxides [20–25], nitrides [26], phosphides [27–29] and chalcogenides [15,30]. Among them, iron doped cobalt sulfides have been

* Corresponding authors.

E-mail addresses: caijy@mail.ustc.edu.cn (J. Cai), samira.siahrostami@ucalgary.ca (S. Siahrostami), wanggm@ustc.edu.cn (G. Wang).

<https://doi.org/10.1016/j.apsusc.2020.148681>

Received 3 September 2020; Received in revised form 24 November 2020; Accepted 2 December 2020

Available online 6 December 2020

0169-4332/© 2020 Elsevier B.V. All rights reserved.

shown to have unique beneficial properties for OER including more abundant donor–acceptor chemisorption sites for reversible adsorption of oxygen [4]. Kong et al. reported that Fe doping resulted in faster kinetic, enhanced intrinsic activity and higher surface roughness of CoS₂ [31]. Zhou et al. identified that the excellent CoFeS OER activity was due to the rate determining step (RDS) changing from first electron transfer to second electron transfer which enhanced the double layer capacitance leading to higher intrinsic activity and lower catalyst electrical resistivity [32]. In addition, transformations of cobalt sulfides, selenides, and nitrides during the OER process have been reported [11,19,30]. The activity of OER catalysts are closely linked to the surface structure of the catalyst. However, there are limited reports on the atomic level active surfaces of Fe doped cobalt sulfides for OER catalysis. More considerations including the effects of the iron fraction in cobalt sulfide, the optimum ratio of Co/Fe, and the surface evolution caused by sulfur dissolution throughout OER process are required.

This study aims at synthesis of Co_xFe_{1-x}S₂ with different Co/Fe atomic ratios to systematically investigate the effects of iron on the electrocatalytic activity of ternary chalcogenides. We successfully dope Fe into cubic cobalt disulfide by introducing trivalent nitrate salts of iron during hydrothermal process and afterwards chemical vapor deposition (CVD) sulfurization treatment. Then electrochemical activation via cyclic voltammetry (CV) is applied to realize a highly active catalytic surface that consist of the amorphous mixed oxide. Impressively, the electrochemical analysis shows that only 267 mV overpotential is required for cobalt iron activated amorphous oxide (Co_xFe_{1-x}-AO) to reach current density of 10 mA cm⁻² and its Tafel slope reduces to 34 mV dec⁻¹. Density functional theory (DFT) calculation identifies the active phase during OER reaction and models for electrochemical water oxidation. This allows us to identify trends of the activity and clarify the reason behind the enhanced activity observed in the experiments.

2. Materials and methods

2.1. Materials

Cobalt nitrate hexahydrate (Co(NO₃)₂·6H₂O), iron nitrate nonahydrate (Fe(NO₃)₂·9H₂O), Urea (CH₄N₂O), Ammonium fluoride (NH₄F), and sublimed sulfur were obtained from Sinopharm Chemical Reagent Co., Ltd. Deionized (DI) water with an electrical resistance of 18.25 MΩ obtained from Ke Ning Te were used in the experiments.

2.2. Synthesis of Co_xFe_{1-x}S₂ and Fe_xCo_{1-x}S₂

First, a piece of carbon cloth (CC) was treated in 66% nitric acid at room temperature for 48 h. Then, the CC was washed thoroughly with ethanol and water several times and dried in an oven at 60 °C for 1 h. Finally, this two solutions were prepared in parallel: about 3 mmol Co(NO₃)₂·6H₂O was dissolved in 50 ml of deionized water, and the same was done on 3 mmol Fe(NO₃)₂·9H₂O. Different volumes of two solutions were mixed together by keeping the total contents at 1 mmol. The following cobalt to iron mixing ratios (Co/Fe) were assembled: 11:1, 5:1, 3:1, and 2:1, which we refer to as Co_xFe_{1-x}S₂-1, Co_xFe_{1-x}S₂-2, Co_xFe_{1-x}S₂-3, Co_xFe_{1-x}S₂-4, respectively. Co_xFe_{1-x}S₂ named in text is Co_xFe_{1-x}S₂-3 where x were calculated from EDX spectra results ($x = \text{Co}/(\text{Co} + \text{Fe}) = 0.84$). The other samples were prepared by addition of iron to cobalt (Fe/Co) at the following fractions: 11:1, 5:1, 3:1, and 2:1, which are denoted Fe_xCo_{1-x}S₂-1, Fe_xCo_{1-x}S₂-2, Fe_xCo_{1-x}S₂-3, Fe_xCo_{1-x}S₂-4, respectively. The prepared solutions were poured into 25 ml Teflon-lined stainless-steel autoclaves containing the pretreated CC and heated in an oven for 6 h at 120 °C.

Finally, the grown catalysts on CC were washed with water and ethanol several times and dried in a vacuum oven at 60 °C for 12 h. As for sulfurization of the aforementioned samples, they were placed in a home-built tube furnace under continuous argon flow with a porcelain crucible filled with 2 g sublimed sulfur placed at the upstream end of the

furnace. The heating rate was set equal to 5 °C min⁻¹ with a maximum temperature equal to 370 °C. The precursors were maintained at this temperature for 60 min and then the furnace was left to cool down to room temperature (this took about 2 h). For pure CoS₂ and FeS₂, the process was conducted without adding Fe(NO₃)₂·9H₂O and Co(NO₃)₂·6H₂O, respectively.

2.3. In-situ activation and transformation of Co_xFe_{1-x}S₂ to Co_xFe_{1-x}-AO and Fe_xCo_{1-x}S₂ to Fe_xCo_{1-x}-AO

A three electrodes system consisting of the catalysts supported on CC as the working electrode, graphite rod as the counter electrode, and Ag/AgCl as the reference electrode were used for electrochemical measurements. The activation process was carried out using cyclic voltammetry (CV) with a scan rate of 5 mV s⁻¹ over 10 cycles for each of the samples, which is optimized by comparing the performance at various cycles. It is expected that activation process transforms the sulfide samples to the corresponding oxides in the catalyst surface layer. It can be seen from Fig. S3 that in first sweep segment from 0 V to 1 V, a huge current density produced before water oxidation because of sulfide oxidation, then from second cycle, it tends to be relaxed and become more stable until reach to tenth cycle, in which no changes in CV cycles can be found.

2.4. Characterization

Morphological characterization of the samples was conducted by using transmission electron microscopy (TEM, JEOL JEM-2010, Japan, 200 kV), High-resolution transmission electron microscopy (HRTEM, JEOL JEM-2100F, Japan, 200 kV) capable of high-angle annular dark-field imaging (HAADF), and field-emission scanning electron microscopy (FESEM, JSM-6700F, 5 kV). Elemental composition was carried out by energy-dispersive X-ray spectroscopy (EDX, Oxford Instruments, Model 7426) coupled to the HRTEM and a scanning electron microscopy (SEM, JSM-5600LV, 15 kV). Crystallographic X-ray diffraction patterns were obtained by powder X-ray diffraction (XRD, Bruker D8 Advance System, Cu Kα radiation at 1.5406 Å). Surface chemical compositions were obtained by X-ray photoelectron spectroscopy (XPS, Synchrotron radiation facility of USTC). The XPS was equipped with monochromatized Al Kα X-ray source ($h\nu = 1286.71$ eV, 5 mA, 15 kV) with a constant analyzer-pass-energy of 40.0 eV, operating at 5×10^{-9} Torr. All binding energies (BEs) were referenced to the C1s peak arising from C-C bonds, and their BE was set at 284.5 eV.

2.5. Electrochemical characterization

The electrochemical measurements were measured on the electrochemical workstation (CHI760E) using a three-electrode electrochemical mode in 1.0 M KOH aqueous solution. The prepared catalysts were served directly as the working electrode, using graphite rod and Ag/AgCl (saturated KCl solution) as counter electrode and reference electrode, respectively. All potentials measured versus Ag/AgCl were converted to reversible hydrogen electrode (RHE) by the following equation: $E(\text{RHE}) = E(\text{Ag}/\text{AgCl}) + 0.197 \text{ V} + 0.059 \text{ pH}$. It should be noted that current density could be obtained from surface oxidation and water oxidation. For reducing impact of surface oxidation on obtained current density, the most stable cycle (in this case tenth cycle) were considered for reported current density. Furthermore, in this CV cycle the reverse sweep segment from 1 V to 0 V were considered for obtaining overpotential at 10 mA cm⁻². Since the catalytic performance of Co-AO is much less than the intentional iron incorporated CoFe-AO measured in the same electrolyte, it means the impurity effect of the electrolyte is negligible.

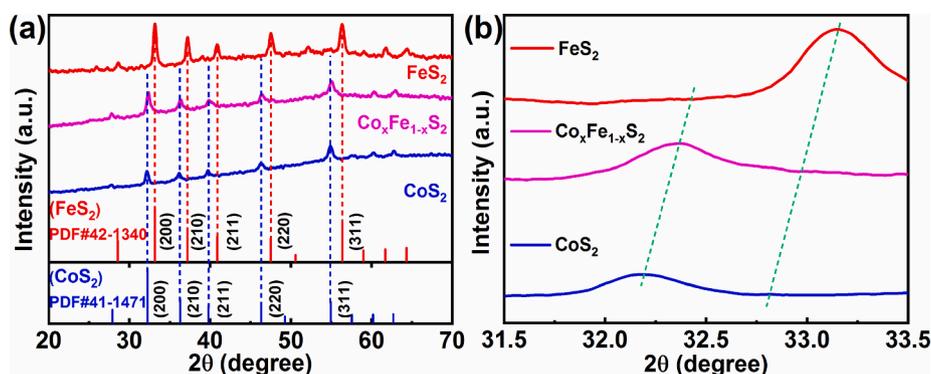


Fig. 1. (a) XRD patterns of CoS_2 , $\text{Co}_x\text{Fe}_{1-x}\text{S}_2$, FeS_2 and (b) magnified XRD patterns in the range between 31.5 and 33.5° .

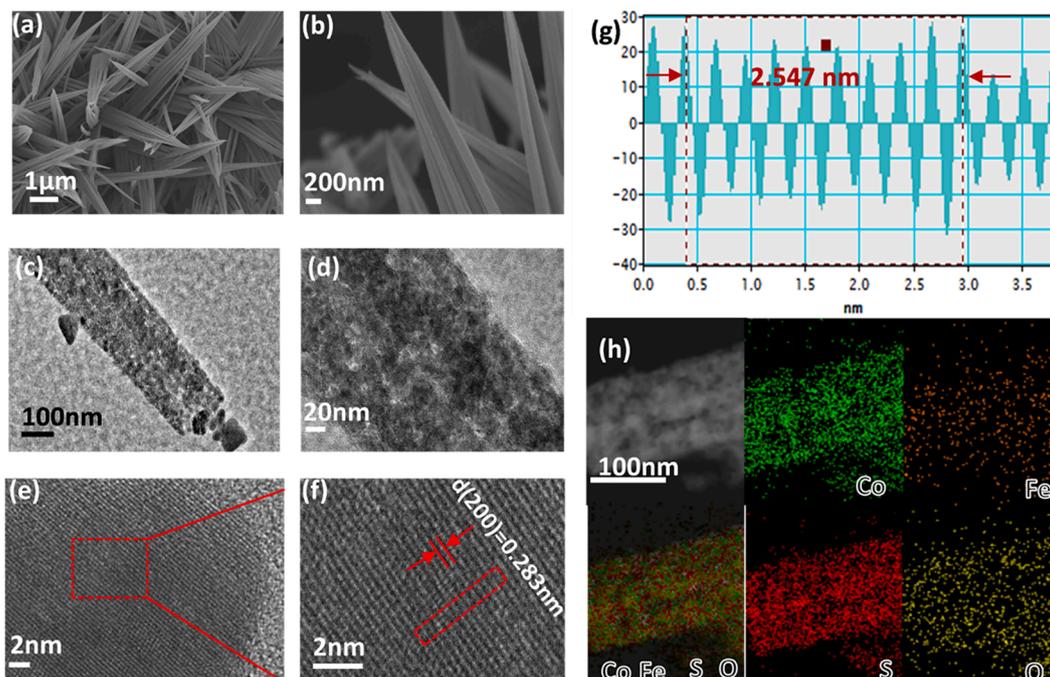


Fig. 2. (a-b) SEM images of $\text{Co}_x\text{Fe}_{1-x}\text{S}_2$ with different magnifications. (c-d) TEM images of $\text{Co}_x\text{Fe}_{1-x}\text{S}_2$. (e-f) HRTEM images and (g) the line profile analysis of $\text{Co}_x\text{Fe}_{1-x}\text{S}_2$. (h) The HAADF-STEM image and elemental mapping images of $\text{Co}_x\text{Fe}_{1-x}\text{S}_2$, respectively. Co (green), Fe (orange), S (red) and O (yellow).

2.6. Density functional theory calculation

Electronic structure calculations were performed using the Vienna Ab initio Simulation Package (VASP) code using projector-augmented wave (PAW) pseudopotentials. The Perdew – Burke – Ernzerhof (PBE) exchange–correlation functional was used. Electron orbitals were expanded by plane wave basis sets with an energy cut-off of 500 eV. For better description of 3d electrons, the value of the effective Hubbard U parameters, $U_{\text{eff}} = 3.32$ eV for Co, $U_{\text{eff}} = 5.33$ eV for Fe were adopted. A 2×2 unit cell with 4-layers thickness was employed with 20 \AA vacuum in the z axis to avoid image interactions. The first two layers of surface atoms as well as the adsorbates were allowed to relax and the bottom two layers of the surface were kept fixed in their bulk position. For sampling, the Brillouin zone consists of a $4 \times 4 \times 1$ k-point mesh. The force on any atoms was converged to less than 0.05 eV \AA^{-1} , while the self-consistency on the total energy for each ionic step was chosen to be $1 \times 10^{-4} \text{ eV atom}^{-1}$. Calculated adsorption energies of the reaction intermediates were used to identify trends in activity for different sulfide structures. The electronic adsorption energies of each OER intermediates were calculated at zero potential and $\text{pH} = 0$, then corrected with zero-point energy (ZPE) and entropy (TS) using $\Delta G = \Delta E +$

$\Delta ZPE - T\Delta S$. The computational hydrogen electrode (CHE) approach was used which assumes that the chemical potential of a proton-electron pair is equal to that of gas-phase H_2 , at $U_{\text{elec}} = 0 \text{ V}$ vs. RHE. The electrode potential is taken into account by shifting the electron energy by $-eU$ where e and U are the elementary charge and electrode potential, respectively.

3. Results and discussions

$\text{Co}_x\text{Fe}_{1-x}\text{S}_2$ and $\text{Fe}_x\text{Co}_{1-x}\text{S}_2$ were synthesized with different amounts of cobalt and iron fractions. The XRD patterns related to all synthesized compounds are depicted in Fig. S1. Fig. 1a presents the XRD patterns of the $\text{Co}_x\text{Fe}_{1-x}\text{S}_2$ along with pure cobalt disulfide (CoS_2), pure iron disulfide (FeS_2), as well as their standard patterns. It can be implied that the $\text{Co}_x\text{Fe}_{1-x}\text{S}_2$ has a similar pattern with CoS_2 (PDF#41-1471), but the positive shift in its peaks is observed in Fig. 1b, as the result of Fe replacing the Co atoms in the cubic structure of CoS_2 [33].

In addition, SEM and TEM were utilized for structural characterization. Fig. 2a and b show the morphology of the synthesized catalysts, which consist of connected nanosized (200nm) wires to form a repetitive network resembling grass. The TEM images shown in Fig. 2c and

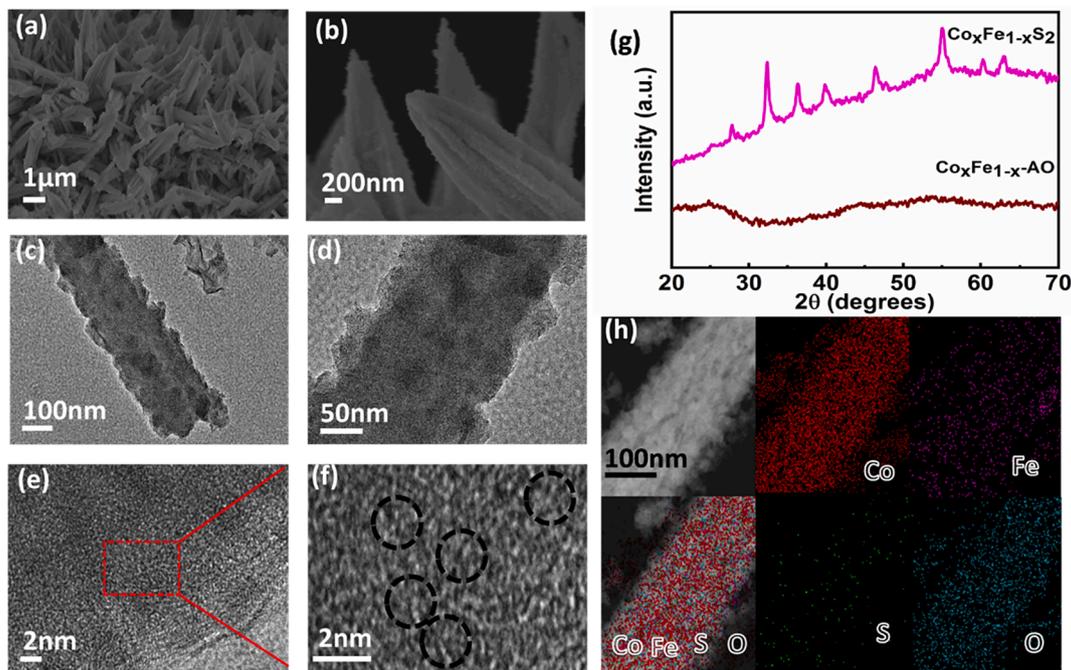


Fig. 3. (a-b) SEM images of $\text{Co}_x\text{Fe}_{1-x}\text{AO}$ with different magnifications. (c-d) TEM images of $\text{Co}_x\text{Fe}_{1-x}\text{AO}$. (e-f) HRTEM images of $\text{Co}_x\text{Fe}_{1-x}\text{AO}$. (g) XRD patterns of $\text{Co}_x\text{Fe}_{1-x}\text{AO}$ obtained before and after activation process, respectively. (h) The HAADF-STEM image and elemental mapping images of $\text{Co}_x\text{Fe}_{1-x}\text{AO}$, respectively. Co (red), Fe (violet), S (green) and O (blue).

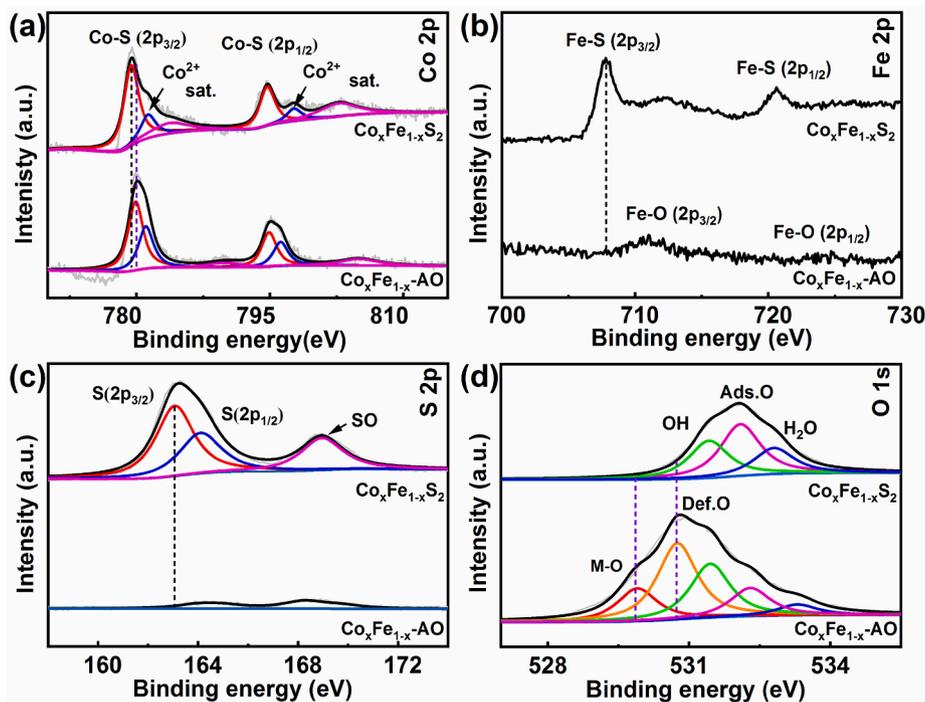


Fig. 4. The high-resolution XPS spectra of (a) Co 2p, (b) Fe 2p, (c) S 2p, (d) O 1s of $\text{Co}_x\text{Fe}_{1-x}\text{S}_2$ (top) and $\text{Co}_x\text{Fe}_{1-x}\text{AO}$ (bottom), respectively.

d present the wire-like structure. Furthermore, HRTEM was used to figure out the extent of crystallinity of $\text{Co}_x\text{Fe}_{1-x}\text{S}_2$. A highly crystalline structure is shown in Fig. 2e-g with d spacing of ~ 0.283 nm, which corresponds to the (200) lattice plane of standard CoS_2 . The energy-dispersive X-ray (EDX) spectrum of $\text{Co}_x\text{Fe}_{1-x}\text{S}_2$ reveals the existence of Co, Fe, S elements (Fig. S2a). Elemental mapping displayed in Fig. 2h reveals that the main elements, including cobalt, iron, and sulfide are distributed homogeneously over the $\text{Co}_x\text{Fe}_{1-x}\text{S}_2$ surface. The presence of

oxygen is due to the oxidation when the samples were exposed to air.

Since high positive potential was applied to anode when CV activation, the catalyst may undergo oxidation. SEM and TEM were also performed to detect structural features of the activated catalyst $\text{Co}_x\text{Fe}_{1-x}\text{AO}$ (activation details in Fig. S3). Fig. 3a and b show the main structural morphology is maintained but the surface of the nanowires becomes rougher. The change of nanowire surface can be more clearly observed by TEM characterization as shown in Fig. 3c and d. HRTEM was further

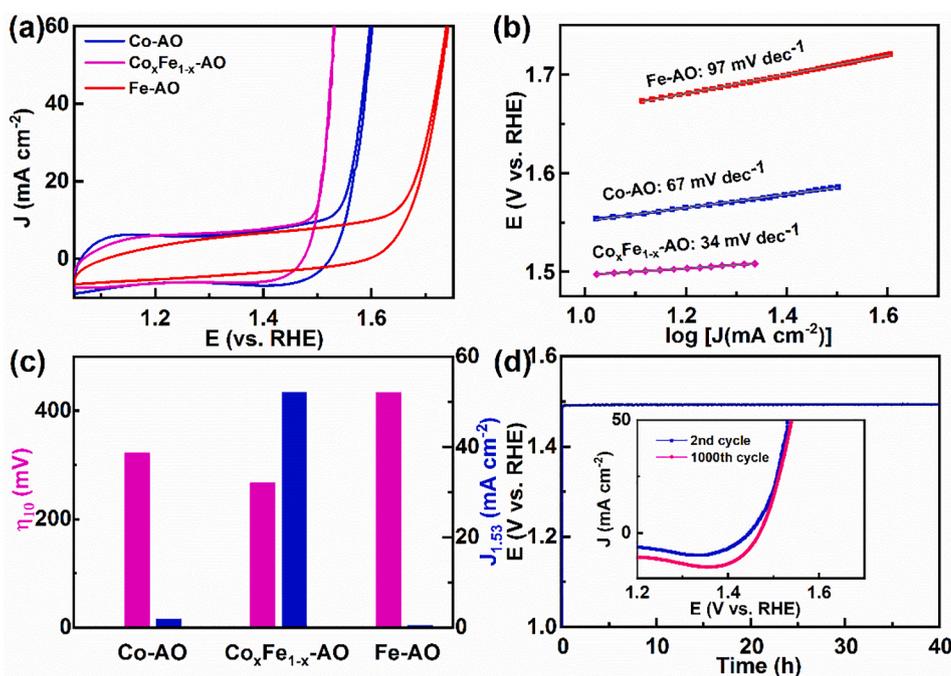


Fig. 5. (a) CV curves with a scan rate of 5 mV s^{-1} in 1.0 M KOH solution for the Co-AO, $\text{Co}_x\text{Fe}_{1-x}\text{-AO}$, Fe-AO, respectively. (b) The corresponding Tafel plots for Co-AO, $\text{Co}_x\text{Fe}_{1-x}\text{-AO}$, Fe-AO, respectively. (c) Overpotentials of Co-AO, $\text{Co}_x\text{Fe}_{1-x}\text{-AO}$, Fe-AO under the current density of 10 mA cm^{-2} and current density obtained at 300 mV overpotential. (d) Chronopotentiometric curve of $\text{Co}_x\text{Fe}_{1-x}\text{-AO}$ recorded for 40 h at 10 mA cm^{-2} vs. RHE, without IR correction. The inset is reverse scan of CV curves for $\text{Co}_x\text{Fe}_{1-x}\text{-AO}$ after first and $1,000$ cycles with scan rate of 100 mV s^{-1} .

performed to characterize the crystallinity of the catalysts after activation process. As shown in Fig. 3e and 3f, the clear lattice fringes of $\text{Co}_x\text{Fe}_{1-x}\text{S}_2$ disappear and present disordered amorphous state. The XRD pattern of $\text{Co}_x\text{Fe}_{1-x}\text{-AO}$ shown in Fig. 3g also indicates that the extent of crystallinity was reduced with an emerging amorphous structure. It is likely that long range disorder structure were formed during the activation process and thus an amorphous pattern appears which is consistent with previously reported works [19]. Moreover, elemental mapping of the post-activated catalyst displayed in Fig. 3h shows a considerable decrease of the sulfur contents of the catalyst with greater oxygen instead. It can be implied that activation causes leaching of the sulfide and its transformation to oxide [19]. The aforementioned results are in a good agreement with the XRD results and together they reveal the surface changes during the activation process.

XPS was further performed to unveil the effect of CV activation on the electronic structures of $\text{Co}_x\text{Fe}_{1-x}\text{S}_2$. Fig. 4a presents the XPS Co spectra of $\text{Co}_x\text{Fe}_{1-x}\text{S}_2$ and $\text{Co}_x\text{Fe}_{1-x}\text{-AO}$, the peaks located at 779.4 and 794.7 eV are associated with the $\text{Co } 2p_{3/2}$ and $\text{Co } 2p_{1/2}$ of Co-S bonds, respectively. After CV activation, these peaks shifted to 780.1 and 795.2 eV which signal the formation of higher oxidized Co on the surface of catalysts which can ascribe to Co-O bonds [34]. The same behavior is also found in Fig. 4b, where the initial peaks are located at 707.7 and 720.5 eV corresponds to Fe-S bonds and the peaks located at 711 and 724.3 eV of $\text{Co}_x\text{Fe}_{1-x}\text{-AO}$ indicate the formation of Fe-O bonds which is mainly from amorphous oxides after CV activation [35]. In Fig. 4c, the doublet peaks at 163.1 and 164.1 eV represent bonding between sulfur and metals and the peak located at 168.9 eV matches to the sulfate group that was formed by oxidation. Obviously, the intensity of peaks declined considerably after activation indicating that the major content of sulfides species was leached into the solution. Fig. 4d shows that the O 1s spectrum comprises three peaks before catalyst reaction at 531.4 , 532.08 , and 532.8 eV , which belong to hydroxyl group, adsorbed oxygen (Ads. O), and water molecules [36], respectively. After the activation step, the intensity of O 1s spectrum is obviously enhanced and two more peaks in comparison with as synthesized catalyst emerged at 529.9 eV and 530.7 eV , which are corresponding to metal-oxygen bonding and oxygen defects (Def. O) respectively. Whereas peaks at 531.4 eV , 532.3 eV , and 533.3 eV are relate to the hydroxyl group, adsorbed oxygen and water on surface of catalyst [35,36]. This further

suggests the formation of surface oxide and O defects after CV activation. From above mentioned characterizations including XRD, XPS and HRTEM, the surface evolution of as-synthesized catalyst was confirmed. The formation of an amorphous oxide with abundant oxygen defects is the feature of this structural transformation as a result of activation process.

The OER catalytic performance of $\text{Co}_x\text{Fe}_{1-x}\text{-AO}$ were evaluated in a typical three-electrode system with 1.0 M KOH solution as the electrolyte. Results of electrochemical studies on all activated catalysts can be seen in Fig. S4. The CV curves and the corresponding Tafel slopes of cobalt sulfide activated amorphous oxide (Co-AO), iron sulfide activated amorphous oxide (Fe-AO) and $\text{Co}_x\text{Fe}_{1-x}\text{-AO}$ are exhibited in Fig. 5a and b. It shows the OER catalytic performance of $\text{Co}_x\text{Fe}_{1-x}\text{-AO}$ is better than that of Co-AO and Fe-AO with Tafel slope of 34 mV dec^{-1} and higher current density at particular potential. Meanwhile, two major parameters are extracted for obvious comparison. One is the required overpotential (η) at 10 mA cm^{-2} , and the other is the current density at 1.53 V vs. RHE (Fig. 5c). The required overpotential to reach 10 mA cm^{-2} is 267 mV for the $\text{Co}_x\text{Fe}_{1-x}\text{-AO}$, which is lower than that for Co-AO (322 mV) and Fe-AO (434 mV). It can be implied that iron doping enhances OER catalytic activity of cobalt disulfide. Moreover, the specific activity estimated by normalizing the current densities based on electrochemical surface area (ECSA) (Fig. S5 and S6) shows the specific current density per catalyst surface area (j_s) of $\text{Co}_x\text{Fe}_{1-x}\text{-AO}$ is consistently higher than that of Co-AO and Fe-AO, suggesting the better OER performance of $\text{Co}_x\text{Fe}_{1-x}\text{-AO}$ than Co-AO and Fe-AO. On the other hand, $\text{Co}_x\text{Fe}_{1-x}\text{-AO}$ obtains the highest current density (52 mA cm^{-2}) at overpotential of 300 mV , which is 35 times higher than that of Co-AO. It shows that iron doping empowers $\text{Co}_x\text{Fe}_{1-x}\text{-AO}$ to reach much higher current densities at lower overpotentials, which is comparable to that of other reported cobalt-iron compounds used in the alkaline OER (Table S1) [19,22–24,31,32,37–39,41–43]. Finally, the long-term chronopotentiometric measurement at 10 mA cm^{-2} was performed to evaluate the electrochemical stability of $\text{Co}_x\text{Fe}_{1-x}\text{-AO}$. Fig. 5d shows that after 40 h continuous electrolysis, the electrocatalyst exhibits nearly the same potential as that obtained at the beginning of the test, indicating that the activated catalyst presents excellent OER activity, along with reasonable long-term stability. The SEM image after stability test shows the nanowire morphology can be maintained (Fig. S7). Moreover, the

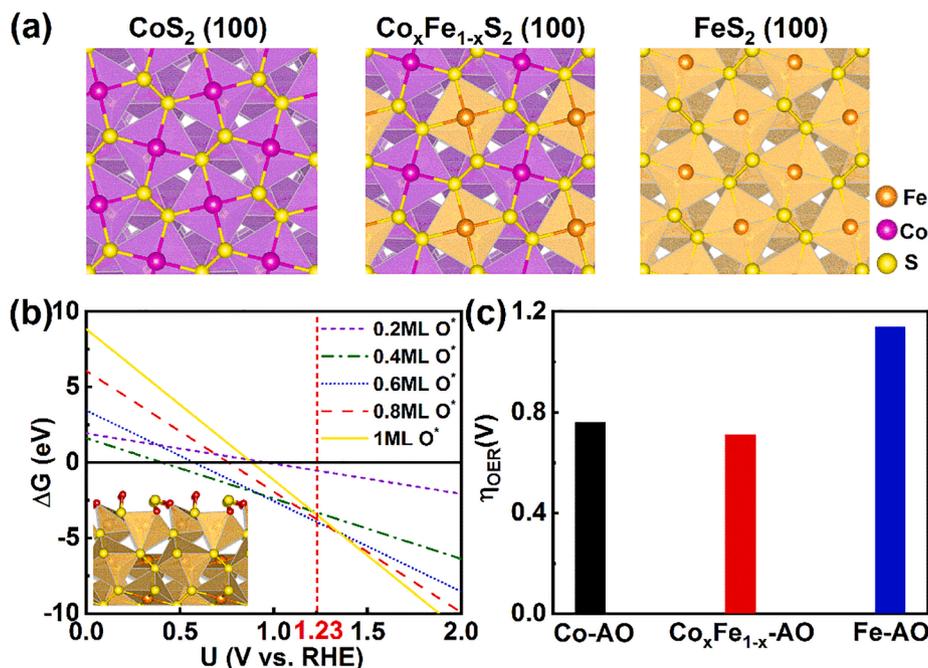


Fig. 6. (a) (100) surface models of CoS₂, Fe-CoS₂, and FeS₂ used in DFT calculations (Co: magenta, Fe: orange, S: yellow). (b) Surface Pourbaix diagram of FeS₂. (c) The calculated OER overpotentials for three systems.

negligible variation of the CV curves after 1,000 cycles demonstrates excellent stability of the Co_xFe_{1-x}-AO catalyst (inset in Fig. 5d). The long-term durability of this catalyst can be attributed to its unique composition and structure. Sulfide leaching caused by the electrochemical activation produce an amorphous oxide surface prohibiting further erosion during stability.

To further confirm the effect of atomic interactions between cobalt and iron on OER catalytic enhancement. We also doped cobalt into iron disulfide. Results in Fig. S8 show that the activity increases considerably when the fraction of cobalt to iron is small (Fe/Co 11:1) and the overpotential decreases from 430 to 350 mV. The current density obtained at 1.53 V increases from 0 to 1.05 mA cm⁻². Additionally, a decrease in obtained Tafel slope from 97 to 66 mV dec⁻¹ suggests the improvement of the OER dynamic when cobalt was incorporated into the iron rich disulfide. The OER catalytic activity of iron-rich disulfides gradually increase by incorporating cobalt until the ratio of Fe to Co reaches 2:1 (293 mV overpotential @ 10 mA cm⁻² and 13.56 mA cm⁻² current density @ 1.53 V vs. RHE). This implies atomic interaction between cobalt and iron contributes to the higher catalytic performance of Fe_xCo_{1-x}S₂ than iron disulfide.

To identify the role of Fe in enhancing OER activity at atomic level, DFT calculations were carried out for simulating OER process on CoS₂, FeS₂, and Fe-doped CoS₂ surfaces. The most stable (100) facets were used for all the model structures (Fig. 6a). To identify the most stable surface coverage under applied potentials, Pourbaix diagrams were constructed. The Pourbaix diagram of FeS₂ displayed in Fig. 6b, and that of CoS₂ both show that at relevant OER potentials (1.23 V and beyond), the surfaces are covered by oxygen [40]. The most stable coverage is one monolayer (1 ML) oxygen, which indicates that the surface is completely oxidized under OER condition. For CoS₂, the S sites are not active, and the most stable structure is Co fully passivated by O. In contrast, FeS₂ has more tendencies toward surface oxidation under OER condition, even the S sites begin to be covered with oxygen. The most stable structures were considered for modeling the OER mechanism. The common associative four electron/proton OER mechanism was adapted. The pH-independent overpotential can be derived from the calculated free energies of ΔG_{O*}, ΔG_{OH*}, and ΔG_{OOH*} intermediates as $\eta_{\text{Theory}} = \frac{\max[4.92 - \Delta G_{\text{OOH}^*}, \Delta G_{\text{OH}^*} - \Delta G_{\text{O}^*}, \Delta G_{\text{O}^*} - \Delta G_{\text{OH}^*}, \Delta G_{\text{OH}^*}]}{e} - 1.23\text{V}$. U_{OER} is define as U_{OER}

= 1.23 V + η_{Theory}. The computed η_{Theory} is given in Fig. 6c. This analysis shows that CoS₂ with a lower η_{Theory} (0.76 V) is more active than FeS₂ (1.14 V). When CoS₂ is doped with Fe, a 0.05 V decrease in η_{Theory} is found. Although our computed values are different from the measured onset potential values in the experiment, the trend of enhanced catalytic performance by Fe-doping is reproduced. For CoS₂ and Fe doped CoS₂, the calculated reaction pathways (Fig. S9-S11) further suggest that Fe doping decrease the energy barrier of the formation of O₂ which is the RDS during the whole OER process. Therefore, the DFT calculation result reveal the thin layer of oxide is the active phase of the OER process and the decreased energy barrier of RDS contributes to the excellent OER performance of Co_xFe_{1-x}-AO.

4. Conclusions

In the current study, Co_xFe_{1-x}S₂ with different ratios of Co to Fe were synthesized as pre-catalyst for OER in alkaline media. It shows that the CV cycling with low scan rate effectively activates the catalyst. The mechanism of the activation process consists of leaching of sulfide and formation of a cobalt-iron amorphous oxide layer on the surface of catalyst. At its optimized Co/Fe ratio, equal to 3:1, the activated catalyst requires only 267 mV overpotential to reach the current density of 10 mA cm⁻². Surface evolution of as-synthesized catalyst to form an amorphous oxide with oxygen defects could increase activity of the catalyst for water oxidation. Furthermore, the results and interpretations from the experiments were proved by DFT calculations in which doping of iron into the CoS₂ raised the activity of the electrocatalyst with decreased overpotential by synergism between the iron and cobalt atoms. From above, it can be concluded that this work could open a new design for OER catalyst by combining structural and compositional modifications.

Declaration of Competing Interest

The authors declare that they have no known competing financial interests or personal relationships that could have appeared to influence the work reported in this paper.

Acknowledgements

A.N. would like to thank the Chinese Academy of Sciences (CAS) and The World Academy of Sciences (TWAS) for awarding him a CAS-TWAS President's PhD fellowship. G.W. and A.N. acknowledge the funding support of the National Natural Science Foundation of China [11722543] and the National Key Research and Development Program of China [2017YFA0206703]. S.S., X.Y., M.K., and I.D.G. acknowledge the support from the University of Calgary's Canada First Research Excellence Fund Program, the Global Research Initiative in Sustainable Low Carbon Unconventional Resources.

Author contributions

G. W. and J. C. designed and supervised the project. A.N. conducted the project. S.S. M.K. and I.G. conceived the DFT calculations. X.Y. and M.K. performed the DFT calculations. Y. Z. helped in XPS measurements and manuscript revision.

Appendix A. Supplementary data

Supplementary data to this article can be found online at <https://doi.org/10.1016/j.apsusc.2020.148681>.

References

- D. Yan, Y. Li, J. Huo, R. Chen, L. Dai, S. Wang, Defect Chemistry of Nonprecious-Metal Electrocatalysts for Oxygen Reactions, *Adv. Mater.* 29 (2017) 1606459.
- N.T. Suen, S.F. Hung, Q. Quan, N. Zhang, Y.J. Xu, H.M. Chen, Electrocatalysis for the oxygen evolution reaction: recent development and future perspectives, *Chem. Soc. Rev.* 46 (2017) 337–365.
- Y. Zhang, Q. Zhou, J. Zhu, Q. Yan, S.X. Dou, W. Sun, Nanostructured Metal Chalcogenides for Energy Storage and Electrocatalysis, *Adv. Funct. Mater.* 27 (2017) 1702317.
- G. Fu, J.M. Lee, Ternary metal sulfides for electrocatalytic energy conversion, *J. Mater. Chem. A* 7 (2019) 9386–9405.
- M. Sun, H. Liu, J. Qu, J. Li, Earth-Rich Transition Metal Phosphide for Energy Conversion and Storage, *Adv. Energy Mater.* 6 (2016) 1600087.
- G. Huang, Z. Xiao, R. Chen, S. Wang, Defect Engineering of Cobalt-Based Materials for Electrocatalytic Water Splitting, *ACS Sustain. Chem. Eng.* 6 (2018) 15954–15969.
- H. Xia, Z. Huang, C. Lv, C. Zhang, A Self-Supported Porous Hierarchical Core-Shell Nanostructure of Cobalt Oxide for Efficient Oxygen Evolution Reaction, *ACS Catal.* 7 (2017) 8205–8213.
- H. Xu, J. Wei, M. Zhang, C. Liu, Y. Shiraiishi, C. Wang, Y. Du, Heterogeneous Co(OH)₂ nanoplates/Co₃O₄ nanocubes enriched with oxygen vacancies enable efficient oxygen evolution reaction electrocatalysis, *Nanoscale* 10 (2018) 18468–18472.
- W. Liu, Y. Hou, Z. Lin, S. Yang, C. Yu, C. Lei, X. Wu, D. He, Q. Jia, G. Zheng, X. Zhang, L. Lei, Porous Cobalt Oxynitride Nanosheets for Efficient Electrocatalytic Water Oxidation, *ChemSusChem* 11 (2018) 1479–1485.
- P. Chen, K. Xu, Z. Fang, Y. Tong, J. Wu, X. Lu, X. Peng, H. Ding, C. Wu, Y. Xie, Metallic Co₄N Porous Nanowire Arrays Activated by Surface Oxidation as Electrocatalysts for the Oxygen Evolution Reaction, *Angew. Chem. Int. Ed.* 54 (2015) 14710–14714.
- Y. Zhang, B. Ouyang, J. Xu, G. Jia, S. Chen, R.S. Rawat, H.J. Fan, Rapid Synthesis of Cobalt Nitride Nanowires: Highly Efficient and Low-Cost Catalysts for Oxygen Evolution, *Angew. Chem. Int. Ed.* 55 (2016) 8670–8674.
- Y. Hao, Y. Xu, W. Liu, X. Sun, Co/CoP embedded in a hairy nitrogen-doped carbon polyhedron as an advanced tri-functional electrocatalyst, *Mater. Horiz.* 5 (2018) 108–115.
- M. Zhai, F. Wang, H. Du, Transition-Metal Phosphide-Carbon Nanosheet Composites Derived from Two-Dimensional Metal-Organic Frameworks for Highly Efficient Electrocatalytic Water-Splitting, *ACS Appl. Mater. Interfaces* 9 (2017) 40171–40179.
- L. Liang, H. Cheng, F. Lei, J. Han, S. Gao, C. Wang, Y. Sun, S. Qamar, S. Wei, Y. Xie, Metallic Single-Unit-Cell Orthorhombic Cobalt Diselenide Atomic Layers: Robust Water-Electrolysis Catalysts, *Angew. Chem. Int. Ed.* 54 (2015) 12004–12008.
- M. Shen, C. Ruan, Y. Chen, C. Jiang, K. Ai, L. Lu, Covalent Entrapment of Cobalt-Iron Sulfides in N-Doped Mesoporous Carbon: Extraordinary Bifunctional Electrocatalysts for Oxygen Reduction and Evolution Reactions, *ACS Appl. Mater. Interfaces* 7 (2015) 1207–1218.
- J. Wang, H.X. Zhong, Z.L. Wang, F.L. Meng, X.B. Zhang, Integrated Three-Dimensional Carbon Paper/Carbon Tubes/Cobalt-Sulfide Sheets as an Efficient Electrode for Overall Water Splitting, *ACS Nano* 10 (2016) 2342–2348.
- X. Ma, W. Zhang, Y. Deng, C. Zhong, W. Hu, X. Han, Phase and composition controlled synthesis of cobalt sulfide hollow nanospheres for electrocatalytic water splitting, *Nanoscale* 10 (2018) 4816–4824.
- S. Li, S. Peng, L. Huang, X. Cui, A.M. Al-Enizi, G. Zheng, Carbon-Coated Co³⁺-Rich Cobalt Selenide Derived from ZIP-67 for Efficient Electrochemical Water Oxidation, *ACS Appl. Mater. Interfaces* 8 (2016) 20534–20539.
- W. Chen, H. Wang, Y. Li, Y. Liu, J. Sun, S. Lee, J.S. Lee, Y. Cui, In Situ Electrochemical Oxidation Tuning of Transition Metal Disulfides to Oxides for Enhanced Water Oxidation, *ACS Cent. Sci.* 1 (2015) 244–251.
- M.S. Burke, M.G. Kast, L. Trotochaud, A.M. Smith, S.W. Boettcher, Cobalt-Iron (Oxy)hydroxide Oxygen Evolution Electrocatalysts: The Role of Structure and Composition on Activity, Stability, and Mechanism, *J. Am. Chem. Soc.* 137 (2015) 3638–3648.
- T. Zhang, M.R. Nellist, L.J. Enman, J. Xiang, S.W. Boettcher, Modes of Fe Incorporation in Co-Fe (Oxy)hydroxide Oxygen Evolution Electrocatalysts, *ChemSusChem* 12 (2019) 2015–2021.
- S.H. Ye, Z.X. Shi, J.X. Feng, Y.X. Tong, G.R. Li, Activating CoOOH Porous Nanosheet Arrays by Partial Iron Substitution for Efficient Oxygen Evolution Reaction, *Angew. Chem. Int. Ed.* 57 (2018) 2672–2676.
- X.F. Lu, L.F. Gu, J.W. Wang, J.X. Wu, P.Q. Liao, G.R. Li, Bimetal-Organic Framework Derived CoFe₂O₄/C Porous Hybrid Nanorod Arrays as High-Performance Electrocatalysts for Oxygen Evolution Reaction, *Adv. Mater.* 29 (2017) 1604437.
- L. Zhuang, L. Ge, Y. Yang, M. Li, Y. Jia, X. Yao, Z. Zhu, Ultrathin Iron-Cobalt Oxide Nanosheets with Abundant Oxygen Vacancies for the Oxygen Evolution Reaction, *Adv. Mater.* 29 (2017) 1606793.
- L.J. Enman, M.B. Stevens, M.H. Dahan, M.R. Nellist, M.C. Toroker, S.W. Boettcher, Operando X-Ray Absorption Spectroscopy Shows Iron Oxidation Is Concurrent with Oxygen Evolution in Cobalt-Iron (Oxy)hydroxide Electrocatalysts, *Angew. Chem. Int. Ed.* 57 (2018) 12840–12844.
- T. Liu, M. Li, X. Bo, M. Zhou, Comparison Study toward the Influence of the Second Metals Doping on the Oxygen Evolution Activity of Cobalt Nitrides, *ACS Sustain. Chem. Eng.* 6 (2018) 11457–11465.
- T. Wang, C. Wang, Y. Jin, A. Sviripa, J. Liang, J. Han, Y. Huang, Q. Li, G. Wu, Amorphous Co-Fe-P nanospheres for efficient water oxidation, *J. Mater. Chem. A* 5 (2017) 25378–25384.
- C. Tang, R. Zhang, W. Lu, L. He, X. Jiang, A.M. Asiri, X. Sun, Fe-Doped CoP Nanoarray: A Monolithic Multifunctional Catalyst for Highly Efficient Hydrogen Generation, *Adv. Mater.* 29 (2017) 1602441.
- Y. Tan, H. Wang, P. Liu, Y. Shen, C. Cheng, A. Hirata, T. Fujita, Z. Tang, M. Chen, Versatile nanoporous bimetallic phosphides towards electrochemical water splitting, *Energy Environ. Sci.* 9 (2016) 2257–2261.
- J.Y. Zhang, L. Lv, Y. Tian, Z. Li, X. Ao, Y. Lan, J. Jiang, C. Wang, Rational Design of Cobalt-Iron Selenides for Highly Efficient Electrochemical Water Oxidation, *ACS Appl. Mater. Interfaces* 9 (2017) 33833–33840.
- W. Kong, X. Luan, H. Du, L. Xia, F. Qu, Enhanced electrocatalytic activity of water oxidation in an alkaline medium via Fe doping in CoS₂ nanosheets, *Chem. Commun.* 55 (2019) 2469–2472.
- Y. Zhou, M. Luo, Z. Zhang, W. Li, X. Shen, W. Xia, M. Zhou, X. Zeng, Iron doped cobalt sulfide derived boosted electrocatalyst for water oxidation, *Appl. Surf. Sci.* 448 (2018) 9–15.
- T. Kinner, K.P. Bhandari, E. Bastola, B.M. Monahan, N.O. Haugen, P.J. Roland, T. P. Bigioni, R.J. Ellingson, Majority Carrier Type Control of Cobalt Iron Sulfide (Co_xFe_{1-x}S₂) Pyrite Nanocrystals, *J. Phys. Chem. C* 120 (2016) 5706–5713.
- C. Yan, G. Chen, X. Zhou, J. Sun, C. Lv, Template-Based Engineering of Carbon-Doped Co₃O₄ Hollow Nanofibers as Anode Materials for Lithium-Ion Batteries, *Adv. Funct. Mater.* 26 (2016) 1428–1436.
- G. Wang, Y. Ling, D.A. Wheeler, K.E.N. George, K. Horsley, C. Heske, J.Z. Zhang, Y. Li, Facile Synthesis of Highly Photoactive α-Fe₂O₃-Based Films for Water Oxidation, *Nano Lett.* 11 (2011) 3503–3509.
- J. Yang, H. Liu, W.N. Martens, R.L. Frost, Synthesis and Characterization of Cobalt Hydroxide, Cobalt Oxhydroxide, and Cobalt Oxide Nanodiscs, *J. Phys. Chem. C* 114 (2010) 111–119.
- Y. Li, J. Yin, L. An, M. Lu, K. Sun, Y.Q. Zhao, D. Gao, F. Cheng, P. Xi, FeS₂/CoS₂ Interface Nanosheets as Efficient Bifunctional Electrocatalyst for Overall Water Splitting, *Small* 14 (2018) 1801070.
- K. Wang, W. Guo, S. Yan, H. Song, Y. Shi, Hierarchical Co-FeS₂/CoS₂ heterostructures as a superior bifunctional electrocatalyst, *RSC Adv.* 8 (2018) 28684–28691.
- J. Du, T. Zhang, J. Xing, C. Xu, Hierarchical porous Fe₃O₄/Co₃S₄ nanosheets as an efficient electrocatalyst for the oxygen evolution reaction, *J. Mater. Chem. A* 5 (2017) 9210–9216.
- W.W. Zhao, P. Bothra, Z. Lu, Y. Li, L.P. Mei, K. Liu, Z. Zhao, G. Chen, S. Back, S. Siahrostami, A. Kulkarni, J.K. Norskov, M. Bajdich, Y. Cui, Improved Oxygen Reduction Reaction Activity of Nanostructured CoS₂ through Electrochemical Tuning, *ACS Appl. Energy Mater.* 2 (2019) 8605–8614.
- P.F. Liu, Y. Shuang, B. Zhang, H.G. Yang, Defect-Rich Ultrathin Cobalt-Iron Layered Double Hydroxide for Electrochemical Overall Water Splitting, *ACS Appl. Mater. Interfaces* 8 (2016) 34474–34481.
- Y.R. Hong, S. Mhin, K.M. Kim, W.S. Han, H. Choi, G. Ali, K.Y. Chung, H.J. Lee, S. I. Moon, S. Dutta, S. Sun, Y.G. Jung, T. Song, H.S. Han, Electrochemically activated cobalt nickel sulfide for an efficient oxygen evolution reaction: partial amorphization and phase control, *J. Mater. Chem. A* 7 (2019) 3592–3602.
- Y. Tang, H. Yang, J. Sun, M. Xia, W. Guo, L. Yu, J. Yan, J. Zheng, L. Chang, F. Gao, Phase-pure pentlandite Ni₄Co₄S₈ binary sulfide as an efficient bifunctional electrocatalyst for oxygen evolution and hydrogen evolution, *Nanoscale* 10 (2018) 10459–10466.